Orographic precipitation and air mass transformation: An Alpine example

By RONALD B. SMITH[1]*, QINGFANG JIANG[1], MATTHEW G. FEARON[1], PIERRE TABARY[2],
MANFRED DORNINGER[3], JAMES D. DOYLE[4] and ROBERT BENOIT[5]

[1]*Yale University, New Haven, USA*
[2]*Centre d'étude des Environnements Terrestre et Planétaires, Vélizy, France*
[3]*University of Vienna, Austria*
[4]*Naval Research Laboratory, Monterey, USA*
[5]*Recherche en prévision numerique, Meteorological Service of Canada, Dorval, Canada*

SUMMARY

A case of orographic precipitation in the Alps on 20 September 1999 was studied using several models, along with rain-gauge and radar data. The objective of the study is to describe the orographic transformation of an air mass, including multi-scale aspects. Several new and some conventional diagnostic quantities are estimated, including drying ratio, precipitation efficiency, buoyancy work, condensed-water residence time, parcel changes in heat, moisture and altitude, and dominant space- and time-scales.

For the case considered, the drying ratio was about 35%. Precipitation efficiency values are ambiguous due to repeated ascent and descent over small-scale terrain. The sign of buoyancy work changed during the event, indicating a shift from stratiform orographic to weak convective clouds. Cloud-water residence times are different for the two mesoscale models (400 compared to 1000 s) due to different cloud–physical formulations. The two mesoscale models agree that the dominant spatial-scale of lifting and precipitation is about 10 km; smaller than the scale of the main Alpine massif. Trajectory analysis of air crossing the Alps casts doubt on the classic model of föhn. Few parcels exhibit classic pattern of moist ascent followed by dry descent. Parcels that gain latent heat descend only briefly, before rising into the middle troposphere. Parcels that descend along the lee slope, originate in the middle troposphere and gain little, or even lose, latent heat during the transit. As parcels seek their proper buoyancy level downstream, a surprising scrambling of the air mass occurs.

Radar data confirm the model prediction that the rainfall field is tightly controlled by local terrain on scales as small as 10 km, rather than the full 100 km cross-Alpine scale. A curious pulsing of the precipitation is seen, indicating either drifting moisture anomalies or weak convection.

KEYWORDS: Föhn   Mesoscale Alpine Programme   Mesoscale model   Mountains   Water budget

1. INTRODUCTION

Orographic precipitation and air mass transformation (OPAT) is the change in water vapour concentration associated with orographic precipitation and the change in potential temperature caused by latent heating. OPAT plays an important role in the earth's climate because of its influence on inter-ocean and meridional water transport, water vapour feedback, coastal rain forests, dry continent interiors and glacier mass balance. It is also important to water resources issues and to the natural hazard of flooding.

The understanding of OPAT has advanced considerably in recent decades. The feeder-seeder mechanism has been investigated by Bergeron (1960), Browning *et al.* (1974) and Bruintjes *et al.* (1994). The roles of the freezing level and cloud-top processes have been studied by Marwitz (1987) and Rauber (1992). The application of numerical modelling techniques to the orographic precipitation problem has been described by Young (1974), Colle *et al.* (1999), Kuligowski and Barros (1999) and Ferretti *et al.* (2000), among others. The nonlinear effect of the cloud physics has been discussed by Jiang and Smith (2003). The dynamical role of airflow blocking and splitting has been studied by Schneidereit and Schär (2000), Rotunno and Ferretti (2001) and Jiang (2001).

* Corresponding author: Department of Geology and Geophysics, Yale University, PO Box 208109, New Haven, CT 06520-8109, USA. e-mail: ronald.smith@yale.edu

Report Documentation Page

Public reporting burden for the collection of information is estimated to average 1 hour per response, including the time for reviewing instructions, searching existing data sources, gathering and maintaining the data needed, and completing and reviewing the collection of information. Send comments regarding this burden estimate or any other aspect of this collection of information, including suggestions for reducing this burden, to Washington Headquarters Services, Directorate for Information Operations and Reports, 1215 Jefferson Davis Highway, Suite 1204, Arlington VA 22202-4302. Respondents should be aware that notwithstanding any other provision of law, no person shall be subject to a penalty for failing to comply with a collection of information if it does not display a currently valid OMB control number.

1. REPORT DATE **25 NOV 2002**	2. REPORT TYPE	3. DATES COVERED **00-00-2002 to 00-00-2002**
4. TITLE AND SUBTITLE **Orographic precipitation and air mass transformation: An Alpine example**		5a. CONTRACT NUMBER
		5b. GRANT NUMBER
		5c. PROGRAM ELEMENT NUMBER
6. AUTHOR(S)		5d. PROJECT NUMBER
		5e. TASK NUMBER
		5f. WORK UNIT NUMBER
7. PERFORMING ORGANIZATION NAME(S) AND ADDRESS(ES) **Naval Research Laboratory,7 Grace Hopper Ave., Stop 2 ,Monterey,CA,93943-5502**		8. PERFORMING ORGANIZATION REPORT NUMBER
9. SPONSORING/MONITORING AGENCY NAME(S) AND ADDRESS(ES)		10. SPONSOR/MONITOR'S ACRONYM(S)
		11. SPONSOR/MONITOR'S REPORT NUMBER(S)

12. DISTRIBUTION/AVAILABILITY STATEMENT
Approved for public release; distribution unlimited

13. SUPPLEMENTARY NOTES

14. ABSTRACT

15. SUBJECT TERMS

16. SECURITY CLASSIFICATION OF:			17. LIMITATION OF ABSTRACT	18. NUMBER OF PAGES	19a. NAME OF RESPONSIBLE PERSON
a. REPORT **unclassified**	b. ABSTRACT **unclassified**	c. THIS PAGE **unclassified**	**Same as Report (SAR)**	**22**	

In spite of these advances, there remains a number of unresolved issues regarding OPAT over complex terrain. First among these is the question of scale. How can one relate the bulk air mass transformation to smaller-scale processes that affect this change?

In order to span these scales we use several tools. The global models of the European Centre for Medium-Range Weather Forecasts (ECMWF) provide forecast and analysis fields on scales of about 40 km. Two mesoscale models are used to provide approximate airflow and cloud fields on scales of 3 and 4 km. The routine Alpine rain-gauge network allows the analysis of a coarse precipitation field on scales of 25 km. The Monte Lema Doppler Radar provides reflectivity, wind fields and precipitation estimates on scales of 3 to 6 km. An additional analysis tool is the high-resolution 'upslope' model, based on the hypothesis that the precipitation is driven by local forced uplift.

To attack such a complex problem we must take advantage of other studies. Our strategy is to describe the Alpine precipitation event of 20 September 1999 during Intensive Observation Period (IOP) 2b of the Mesoscale Alpine Programme (MAP, Bougeault *et al.* 2001). Precipitation and föhn in the Alpine region have been studied more intensely than in any other part of the world (e.g. Seibert 1990; Haimberger *et al.* 1995; Buzzi *et al.* 1998; Doswell *et al.* 1998; Frei and Schär 1998; Ferretti *et al.* 2000; Mladek *et al.* 2000; Schneidereit and Schär 2000; Rotunno and Ferreti 2001). In addition, this particular event is the most widely studied of all MAP cases. The reader can find several papers in this volume that will add detail and context to our description (e.g. Doyle and Smith 2003).

In sections 2 and 3, the models and the meteorological events of 20 September 1999 are described. The analysis is divided into three parts. In section 4, we use volumetric and flux integrals to characterize the water budget, air mass transformation, cloud residence time and precipitation efficiency in test boxes. In section 5, we examine how air mass transformation occurs on individual air parcels crossing the Alps. In section 6, we use radar data to test the model predictions of scale. Our findings are summarized in section 7.

2.   MESOSCALE MODELS

Two mesoscale models are used here to generate fields for analysis: the Meso-scale Compressible Community Model (MC2, Benoit *et al.* 1997) and the Coupled Ocean Atmosphere Mesoscale Prediction System (COAMPS, Hodur 1997). Details are given in Table 1. The use of two models allows us to identify robust features in the predicted fields. Both models are primitive-equation non-hydrostatic models with explicit microphysics, including ice phase processes. The models are run without cumulus parametrization. Both models are nested into larger-scale forecast models and both successfully captured the basic timing and structure of the IOP 2b events. MC2, in spite of its slightly smaller grid cell (3 km), uses a terrain that is smoother than COAMPS. It is difficult to judge the importance of still smaller-scale unresolved terrain. Only a small part of the hydrostatic vertically propagating wave spectrum remains unresolved. The COAMPS model has been tested against aircraft data for other MAP events (Smith *et al.* 2002) and for the event studied here (Doyle and Smith 2003). MC2 was used during the MAP Special Observing Period to produce forecast guidance for the field deployments (Benoit *et al.* 2002). The reader can find further discussion of model performance in other papers in this special MAP volume.

A useful reference model of orographic precipitation is the upslope-time-delay model proposed by Smith (2003) (hereafter UTD model), including microphysical time lags. This model assumes that cloud water is generated over windward slopes

TABLE 1. CHARACTERISTICS OF TWO MESOSCALE MODELS

Aspect	COAMPS	MC2
Horizontal grid resolution	4 km	3 km
Vertical resolution	30 levels on terrain-following coordinates	50 levels on terrain-following coordinates
Boundary conditions	80 km NOGAPS[1] forecast fields for outer mesh. Triple nested: grid sizes 36, 12 and 4 km	14 km Swiss Model forecast fields
Cloud physics scheme	Rutledge and Hobbs (1983)	Kong and Yau (1997)
Condensed-water species	Cloud water, cloud ice, snow and rain	Cloud water, snow, graupel and rain
Atmospheric boundary layer	1.5 order turbulence kinetic energy closure (Mellor and Yamada 1974)	Prognostic equation for turbulent kinetic energy (Benoit *et al.* 1997)

[1] Navy Operational Global Atmospheric Prediction System.

in proportion to wind speed and terrain slope. The vertically integrated generation of supersaturated water vapour (in kg m^{-2}s^{-1}) by forced moist ascent is approximated by

$$S(x, y) = \rho q_{vs} \, \text{Max}(\mathbf{U} \cdot \nabla h, 0), \qquad (1)$$

where x, y are Cartesian coordinates, $\rho(x, y)$ and $q_{vs}(x, y)$ are the surface air density and saturation specific humidity, $\mathbf{U}(x, y)$ is the horizontal wind velocity vector and $h(x, y)$ is the terrain (Smith 1979). Negative 'downslope' values are set equal to zero. To address questions of scale, we allow a time delay between cloud generation and precipitation, following Smith (2003). The double Fourier transform of the precipitation $P(x, y)$ and cloud-water generation $S(x, y)$ are related by

$$\widehat{P}(k, l) = \frac{\widehat{S}(k, l)}{(1 + i\sigma \tau_c)(1 + i\sigma \tau_f)}, \qquad (2)$$

where k and l are horizontal wave number components, τ_c is the conversion time for hydrometeor formation, τ_f is the fallout time, and the intrinsic frequency is $\sigma = Uk + Vl$, where U and V are the zonal and meridional velocity components.

Examples of predictions from the different models are shown in Figs. 1–4. Figure 1 shows the wind and specific-humidity fields 500 m above ground level from COAMPS for 06 UTC; it illustrates the drying of the southerly flow as it crosses the Alps. Figure 2 compares the incoming moisture-flux densities from COAMPS and MC2 along 45.5° latitude at 08 UTC. The two flux-density fields are similar, but the MC2 flux is more concentrated between 8 and 10°E. The daily total precipitation patterns predicted by the three models are shown in Fig. 3. Gridded values represent the sum of 24 hourly values. For the UTD model, the generation rate (1) at each hour is computed from the COAMPS surface q_{vs} field and a horizontal wind vector averaged from the ground to 5 km*. Delay times of 500 s were used in (2), with a horizontal wind vector ($U = 4.8$ m s^{-1}, $V = 14.1$ m s^{-1}) computed by averaging COAMPS fields over the box. A corresponding computation based on the MC2 model (not shown) gives very similar results, but is slightly smoother due to the smoother terrain used. The predicted patterns are qualitatively similar for all three models. Each model result shows strong control by complex terrain on scales of 5 to 20 km. By contrast, the gridded rain-gauge data (Fig. 3(d)) is very smooth (C. Frei and E. Häller, private communication). Finally, in Fig. 4 we compare various flux and mass computations between the two models. At least for water flux, precipitation, and cloud and rain amounts, the models agree within a factor of two or better.

* Altitudes in this paper are above mean sea level unless stated otherwise.
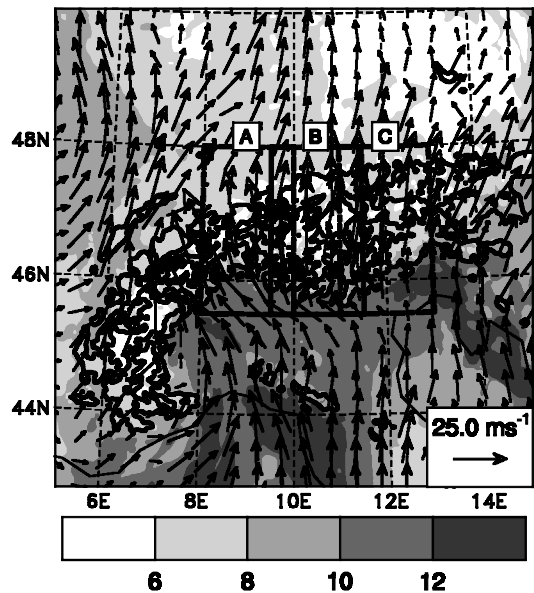
Figure 1.   Plan view of Alpine flow at 06 UTC 20 September 1999 showing the COAMPS low-level specific humidity (shaded, g kg^{-1}) and wind field at 50 m above ground level. Also shown are boxes A, B and C used in budget analyses. The topography contour interval is 1000 m. Strong moist southerly flow approached the Italian Alps; the dry area in the north-east is caused by the drying action of the Alps. See text for details of model.
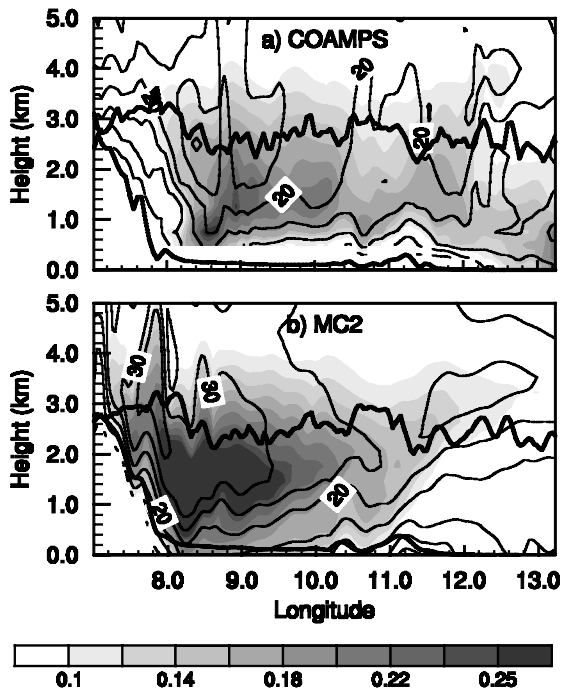

Figure 2.   Incoming water vapour flux density (shaded, kg m^{-2}s^{-1}) and northerly wind component (contoured, m s^{-1}) through a vertical plane along 45.5°N at 08 UTC 20 September 1999 for models: (a) COAMPS, (b) MC2. Terrain in the plane of the cross-section is shown, along with the projected crestline of the Alpine massif. The area-integrated water vapour flux is given in Table 1 and Fig. 4. See text for details of models.
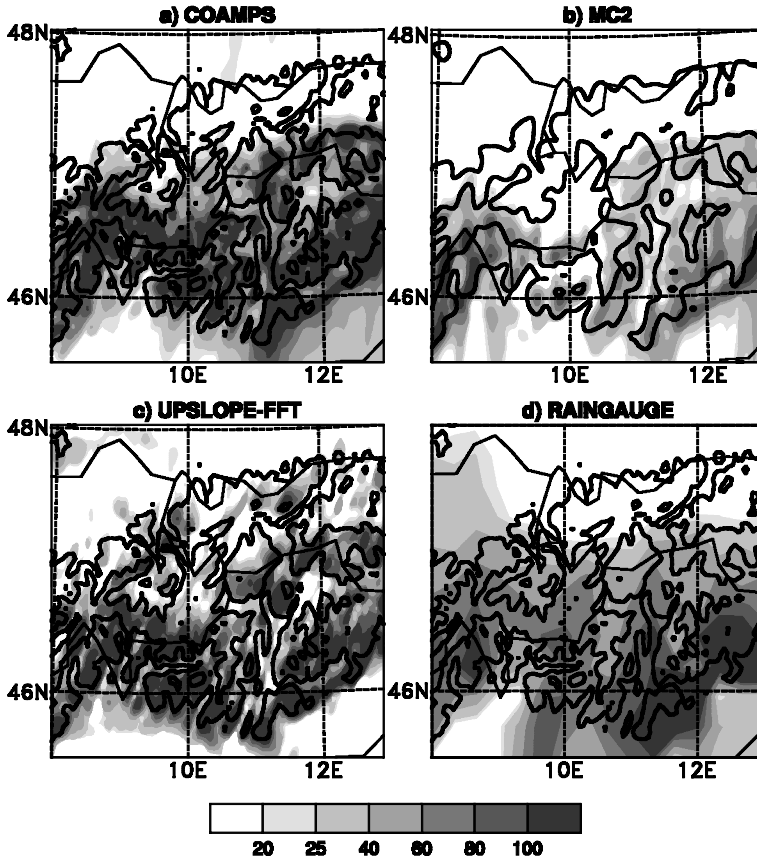
Figure 3. Accumulated daily total precipitation (shaded, mm) for 20 September 1999 over the central Alps for models: (a) COAMPS, (b) MC2, (c) UTD ($T_c = T_f = 500$ s, U, $V = 4.8$, 14.1 m s^{-1}, values divided by 5), (d) smoothed station data (Frei and Häller, personal communication). COAMPS 1 and 2 km terrain contours are shown in (a), (c) and (d), whilst (b) shows the same for MC2. See text for further details.

3. THE 20 SEPTEMBER 1999 IOP 2B CASE

IOP 2b on 20 September 1999 has been studied by several MAP researchers (e.g. Gheusi 2001; Doyle and Smith 2003) so a detailed synoptic description is not given here. It was the strongest precipitation event that occurred in the Italian Alps during the MAP field phase and was associated with significant flooding. The salient aspect of the event was an eastward drifting front and associated moist southerly jet impinging on the Italian Alps. This airstream was moistened by evaporation over the Mediterranean and Adriatic Seas. As it came ashore over the Italian coast, some moisture was lost from the jet by orographic precipitation in the coastal Alps near Nice and the coastal Apennines near La Spezia, but the jet was still quite moist when it reached the main Alpine massif. In contrast, the air to the north of the Alps was dryer due to orographic air mass transformation (Fig. 1). The IOP 2b case was similar in some respects to the well-known Piedmont flash flood event in 1994 (e.g. Buzzi *et al.* 1998)

The vertical structure of the incoming moist jet at 45.5°N at 08 UTC is shown in Fig. 2. The northward moisture-flux density in units of kg m^{-2}s^{-1} is shown. The moisture flux is mostly concentrated below 3 km. The projected ridge-line of the Alps
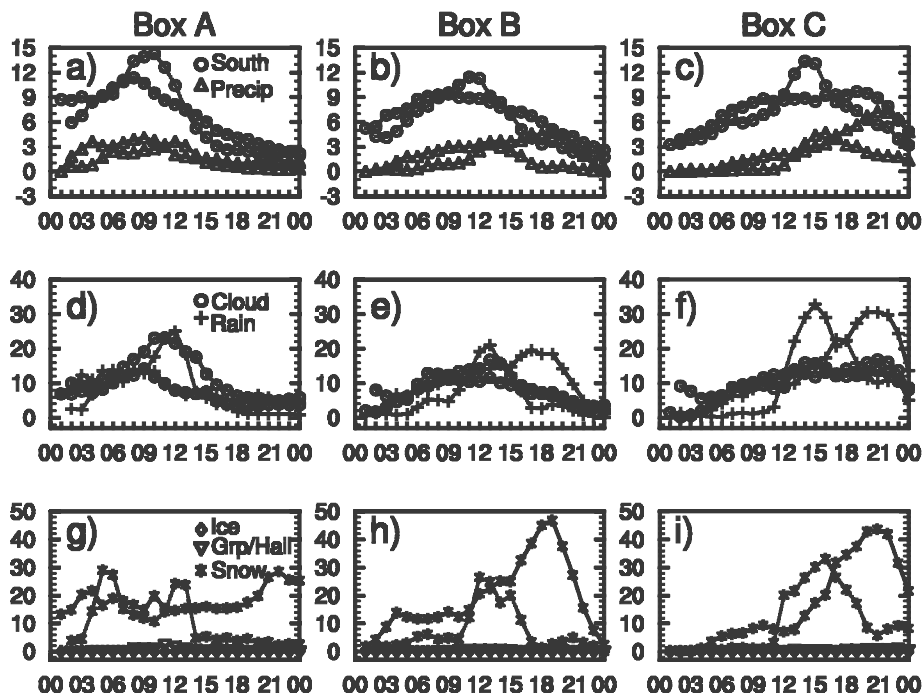
Figure 4.   Water vapour flux, precipitation and volume integrals versus time (UTC) from models COAMPS (solid line) and MC2 (dashed line) for boxes A, B and C (see Fig. 1). Hourly values during 20 September 1999 are shown with flux and volume integrals taken up to 5 km: (a), (b) and (c) northward water vapour flux through the southern boundary and box-total precipitation (units 10^7 kg s^{-1}) for boxes A, B and C, respectively; (d), (e) and (f) volume integrated cloud water and rain (units 10^9 kg) for both models for boxes A, B and C; (g), (h) and (i) volume integrated snow and minor species of cloud ice (for COAMPS, units 10^9 kg) and graupel (for MC2, units 10^9 kg) for boxes A, B and C. The water vapour flux peak at 07 to 11 UTC in Box A shifts to later times in Boxes B and C as the front moves eastward. The precipitation peak lags the influx by a few hours. See text for details of models.

in Fig. 2 shows how much lifting will be required for this jet to cross the Alps. As the jet translated eastward, the region of precipitation shifted along the Alpine foothills from Lago Maggiore to Verona and then to the Friuli area. By the end of the day, the precipitation totals were spread uniformly east-to-west along the Italian Alps, although locally modulated by mesoscale terrain (Fig. 3). The control volumes in this study comprise the large box from 45.5 to 48°N and between 8 and 13°E, and the three sub-boxes: Box A (8 to 10°E), Box B (9.5 to 11.5°E), and Box C (11 to 13°E) shown in Fig. 1; the Boxes extend from the ground to height $z = 5$ km. The time sequence of events can be illustrated using the fluxes coming into, and the precipitation within, Boxes A, B and C (Fig. 4) which are computed in the next section. In Box A, the incoming water vapour flux and precipitation were strong from 02 to 11 UTC. Observers reported that skies began to clear by 18 UTC. In Box C, the flux and precipitation rates were largest in the afternoon hours (Fig. 4).

The role of convection during IOP 2b is somewhat uncertain. During MAP IOP 2a on 17–18 September 1999, just two days before IOP 2b, convection was triggered over the Italian Alps by a moving mid-level trough (Tabary, personal communication). An attempt to characterize the environment for convection is shown in Fig. 5. We computed the difference between the equivalent potential temperature at 5 km and the surface. A large positive value indicates moist stability. In Box A, the southerly inflow turned from
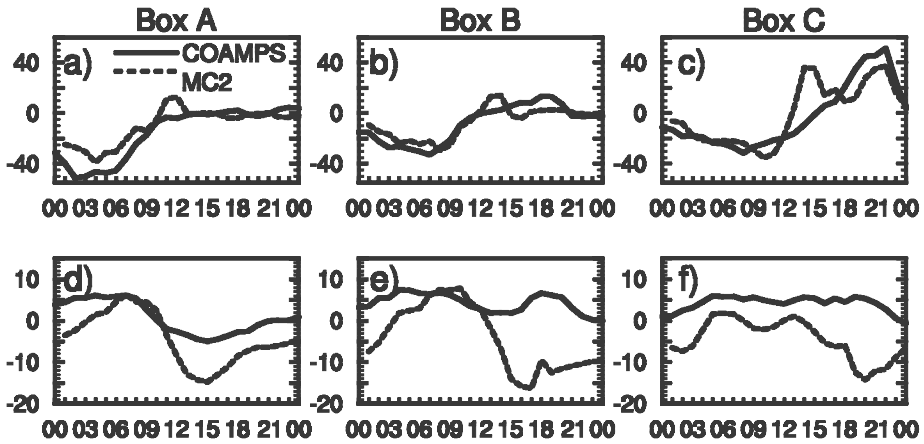
Figure 5. Hourly values of convection diagnostics from models COAMPS (solid) and MC2 (dashed) during 20 September 1999: (a), (b), and (c) the buoyant work within boxes A, B and C, respectively, computed from the volume integral of $\rho w'T'$ (units 10^{12} kg m s^{-1}K, see Eq. (3)); (d), (e) and (f) the incoming moist stability defined as the equivalent potential-temperature difference (K) between 5 km and the surface for each box. In the afternoon, stability decreases and buoyant work increases. See text for further details and Fig. 1 for location of boxes.

slightly stable to significantly unstable after 11 UTC. A similar destabilization of the inflow occurred in Boxes B and C at later times. This trend is clear in MC2 but barely evident in the COAMPS fields.

In order to quantify the intensity of convection over the Alps, and measure the dominance of orographic precipitation, we computed the rate of buoyant generation of turbulent kinetic energy in each box. According to the classical föhn concept, the descending dry air is warmer than the ascending moist air, giving negative buoyancy work. In contrast, classical thermal convection requires warm ascent and cool descent. Buoyant work was estimated by integrating the product $\rho w'T'$, up to 5 km (Fig. 5), where T' is the temperature perturbation and w' is the perturbation of vertical motion. In the absence of other processes,

$$\mathrm{d}(TKE)/\mathrm{d}t = g\rho \iiint w'T' \, \mathrm{d}x \, \mathrm{d}y \, \mathrm{d}z, \tag{3}$$

where TKE is the turbulent kinetic energy. T' was computed by subtracting the box average temperature at each level.

The time series from both models and in all three boxes are similar (Fig. 5). The buoyant work is initially negative, an indication of classical föhn. During this period, the patterns of vertical velocity at height $z = 5$ km are mostly linear wave-like features aligned with the terrain. In the afternoon, the energy conversion becomes positive, especially in Box C. Examination of the evening vertical velocity fields at $z = 5$ km showed few wave-like features; instead, widespread randomly distributed regions and lines of upward velocity are seen, especially in the Box C area, suggestive of weak convection. In spite of this evidence of convection in the models, we believe that the accumulated-precipitation patterns are still dominantly controlled by orographic uplift (Fig. 3).

4.   ANALYSIS OF FLUX AND VOLUME INTEGRALS

(a)   *Water budgets*

An understanding of OPAT requires quantitative estimates of the components of the water budget in the air column above the mountain range. Previous attempts to construct Alpine water budgets directly from upper-air soundings alone have shown limited skill (Haimberger *et al.* 1995). In the current study, we hypothesize that water vapour fluxes can be better determined using mesoscale and global models. The mass and moisture flux fields in these models arise from four-dimensional assimilation of data from sounding stations. The models themselves conserve both air mass and water. These fluxes are carried accurately from the outer grid to the nested model. The primary uncertainties in flux calculations from models arise from initial-condition errors, physical parametrizations, boundary conditions and humidity biases in the rawinsonde data.

The fluxes of water vapour through the north and south facing sides of the Boxes are computed from

$$F = \iint \rho q_v V \, \mathrm{d}x \, \mathrm{d}z, \tag{4}$$

where ρ is the air density and q_v is the specific humidity. The integral (4) is computed after the model fields are interpolated to a Cartesian grid. The total amount of water vapour in a box is computed from

$$M = \iiint \rho q_v \, \mathrm{d}x \, \mathrm{d}y \, \mathrm{d}z. \tag{5}$$

A similar formula is used for the condensed phases. For 20 September, we computed the hourly water vapour fluxes for all the boundaries of each box shown in Fig. 1 and the water content for each phase of water. Both mesoscale models were used, as well as the six-hourly ECMWF forecast and analysis. As a test of our interpolation procedure, mass conservation was evaluated by summing all the boundary fluxes. Imbalance errors varied from 1% to 5% of the largest flux component depending on the interpolation scheme used. Similar errors are expected in the water fluxes.

The dominant water-vapour fluxes are plotted in Fig. 4 and listed in Table 2. Because of the predominance of southerly flow in this case, the fluxes through the east- and west-facing sides are less significant than those through the north and south boundaries. The water flux through the box top is fairly small and not discussed here.

The fluxes of water vapour in through the southern boundary (row (a)) and out through the northern boundary (row (b)) are rather consistent across the four models (Table 2). For Box A, estimates of the influx of water vapour vary from 42×10^{11} to 56×10^{11} kg. The model precipitation values vary more noticeably (row (c)). The highest precipitation was predicted by COAMPS, followed by ECMWF forecast and MC2. For Box A, COAMPS predicted a precipitation of 19×10^{11} kg while MC2 predicts 12×10^{11} kg.

Two values for rain-gauge precipitation are given in row (d): the first value comes from the analysis by Frei and Häller (private communication from the MAP Data Center in Zurich); the second is from the Vienna Enhanced Resolution Analysis (VERA), run by the University of Vienna. The two values are nearly identical, but both may be in error because of a valley bias in the rain-gauge sites. If this is a significant factor, the estimates in row (d) may be too low. The rain-gauge data apply to the period 06 to 06 UTC for the estimates by Frei and Häller, while VERA and the model-derived values pertain to the period from 00 to 24 UTC. The six-hour timing difference introduces only a small error as most of the precipitation occurs in the middle of the day.

TABLE 2. WATER FLUXES, PRECIPITATION AND NON-DIMENSIONAL RATIOS
DERIVED FROM FOUR MODELS FOR 20 SEPTEMBER 1999

Row	Quantity	Box A	Box B	Box C
(a)	*WV* influx (4)	56/53/42/44	55/48/48/49	69/59/58/57
(b)	*WV* outflux (4)	33/35/33/29	34/37/39/31	38/39/45/35
(c)	Model *P*	19/12/17	22/9/18	26/14/19
(d)	Rain-gauge *P*	19 (19)	22 (23)	24 (23)
(e)	Upslope *P* (1)	95/108	98/112	96/105
(f)	*DR* (c)/(a)	34/23/40	40/19/38	38/24/33
(g)	*DR* (d)/(a)	34/36/45/43	40/46/46/45	35/41/41/42
(h)	*PE* (c)/0.36(a)	95/64/101	112/53/112	106/67/98
(i)	*PE* (d)/0.36(a)	94/100/126/120	112/127/127/125	97/113/115/117
(j)	*PE* (c)/(e)	20/11	22/8	27/13

The models are COAMPS, MC2, and ECMWF forecast, together with the ECMWF
analysis; values are given in that order separated by forward slashes. Water vapour
(*WV*) flux and precipitation values (*P*) are accumulations over 24 hours, in units
of 10^{11} kg. Non-dimensional ratios—drying ratio (*DR* Eq. (6)), and precipitation
efficiency (*PE*, Eq. (7))—are given as percentages. The ECMWF analysis does not
include precipitation estimates. Actual precipitation values are estimated from Frei and
Häller, and VERA in parentheses. Boxes A, B and C are shown in Fig. 1. See text for
further details.

The precipitation estimate in row (e) of Table 2 comes from the upslope equation
(1) using the low-level specific humidity and the vertically integrated winds (surface
to 5 km) from COAMPS and MC2. This estimate is very high, for two reasons: first,
it assumes that all upslope currents penetrate up through the moist layer; second,
it adds all positive upslope contributions, failing to account for evaporation during
descent. Surprisingly, the upslope generation of cloud water from (1) ($\sim 100 \times 10^{11}$ kg)
is roughly double the incoming water vapour flux ($\sim 55 \times 10^{11}$ kg). This apparent
contradiction arises from the repeated ascent and descent over multiple ridges as the
air climbs over the Alpine massif. This result is a characteristic feature of orographic
precipitation over complex terrain; the same water molecules condense over and over
again.

We define the drying ratio (*DR*) as the ratio of the precipitation to the incoming flux
of water vapour.

$$DR = P/WV \; Influx. \tag{6}$$

DR values are given in Table 2, row (f), for all models and three Boxes. As the two
mesoscale models have similar incoming fluxes but different precipitation rates, their *DR*
values are different. The COAMPS values (i.e. 34 to 40%) are probably more believable
than the MC2 values, as the COAMPS net precipitation is closer to the observed values.
It also agrees well with the ECMWF forecast estimates, made on a much coarser grid.
When *DR* is recalculated using observed precipitation (row (g)) the values are quite
consistent; ranging between 34% and 46%.

The precipitation efficiency (*PE*) is defined as the ratio of the rates of precipitation
and cloud-water generation.

$$PE = P/Cloud\text{-}water \; generation \tag{7}$$

Various estimates of *PE* are given in Table 2, rows (h), (i) and (j). These values differ
considerably because the cloud-water generation rate is difficult to estimate, and to some
extent it is an ambiguous quantity. The simplest way to compute *PE* is to assume a
smooth pseudo-adiabatic lifting of the incoming air mass by 2 km (see Fig. 2). In the
range of temperatures appropriate here, this process would condense about 36% of the
water vapour. *PE* values computed in this way using the incoming flux (Table 2, row

TABLE 3.   MICROPHYSICAL VOLUME INTEGRALS FOR COAMPS AND MC2 FOR 20 SEPTEMBER 1999

Row	Quantity Times (UTC)	Box A 00–12	12–24	Box B 00–12	12–24	Box C 00–12	12–24
(a)	Precipitation	30/22	13/06	21/10	30/09	10/4	49/27
(b)	Cloud	10/16	4/8	9/11	7/7	8/9	12/14
(c)	Rain	11/13	6/3	9/7	12/4	6/4	21/17
(d)	Snow	18/16	20/4	14/8	26/6	5/4	29/17
(e)	$T_t = [\{(b) + (c) + (d)\}/(a)]$	13/20	23/25	15/26	15/19	19/42	13/18
(f)	$T_c = \{(b)/(a)\}$	3/7	3/13	4/11	2/8	8/23	2/5

Row (a) is average precipitation rate in 10^6 kg s^{-1}; rows (b), (c), (d) are average masses of condensed water in 10^9 kg; rows (e) and (f) give residence time in 10^2 s (see Eqs. (8) and (9)). Values from models COAMPS and MC2 are separated by a forward slash. Boxes A, B and C are shown in Fig. 1.

(a)) and the model precipitation (row (c)), are equal to the *DR*s (row (f)) divided by 0.36 (row (h)). The values are nearly 100% for COAMPS and the ECMWF forecast, but only about 60% for MC2 because of its lower precipitation. The *PE* values computed from the actual precipitation (row (d)) are shown in row (i). Some of these values slightly exceed 100%.

A third way to compute *PE* is to use the UTD model, (1) and Table 2 row (e), to estimate the rate of cloud-water generation. These *PE* values (row (j)) are small, in the range from 8 to 27%, due to the overestimation of condensation rate. The low *PE* values are a reminder of the scale-dependence of this diagnostic quantity. The *PE* values in Table 2 can be compared with estimates from other mountain ranges and conditions (Smith 1979; Hill *et al.* 1981).

(*b*)   *Residence times*

Estimates of the residence times for condensed water can be obtained from volume integrals of condensed species. Hourly values of condensed mass are plotted in Fig. 4. Twelve-hour averages are given in Table 3 for COAMPS and MC2 over the three Boxes, for two time periods. The timing of events seen in Fig. 4 is also seen in Table 3. For example, in Box A, a significant drop in precipitation and condensed-water mass is seen between the morning and afternoon.

In a system this complex, residence times can be defined in several different ways. For simplicity, we define T_c as the ratio of the volume-integrated cloud water (Table 3, row (b)) to the area-integrated precipitation rate (Table 3, row (a)).

$$T_c = Cloud\text{-}water\ amount/Precipitation\ rate. \tag{8}$$

This choice implicitly assumes that precipitation is the dominant loss mechanism. This is not self-evident as evaporation may also be significant. The results for the two models are quite different (Table 3, row (f)); COAMPS gives times in the range 200 to 800 s while MC2 values range from 500 to 2300 s. This difference indicates that MC2 is much slower to convert cloud water to precipitation. As the incoming fluxes for the two models are similar (Table 2), this T_c difference may explain the higher precipitation predicted by COAMPS.

A further indication of microphysical efficiency is the characteristic time for all condensed water to fall as precipitation,

$$T_t = Total\ condensed\ water/Precipitation\ rate. \tag{9}$$

Values of T_t range from 1300 to 2300 s for COAMPS and 1900 to 4200 s for MC2 (Table 3, row (e)).

The relationship between microphysical time-scales (8) and (9), and precipitation efficiency (7) has been investigated by Jiang and Smith (2003). In their linear control-volume model, the dependence of precipitation efficiency on mountain-scale is captured in the expression

$$PE = 1/(1 + \tau_c/\tau_a)(1 + \tau_f/\tau_a), \tag{10}$$

where the mountain-crossing time-scale $\tau_a = a/u$ is the ratio of mountain half-width (a) to wind speed (u). The microphysical time-scale for conversion of cloud water to hydrometeors (τ_c) and for fallout (τ_f) appear as parameters in (10). We consider two cases with half widths equal to 5 and 50 km. If we choose $u = 20$ m s^{-1}, and $\tau_c = \tau_f = 500$ s (from Table 3, row (f)) these cases give $PE = 11\%$ and 69%, respectively. The former small value of PE may explain the overestimation of precipitation by the UTD model. For narrow ridges, there is insufficient time for cloud water to convert and fall, before descent and drying begin. The water vapour will condense again on the next ridge. A wider mountain, or multiple encounters with narrow hills, will eventually remove significant water from the air mass.

5. TRAJECTORIES AND AIR MASS TRANSFORMATION

The bulk aspects of air mass transformation were examined in section 4 using flux calculations, but these thermodynamic processes are better illustrated by following air parcels across the mountains. Tracking parcels, we can test the textbook model of orographic precipitation and föhn.

We computed several dozen air-parcel trajectories from the COAMPS simulation, starting along the 45.5°N latitude line, at a variety of different longitudes (from 8 to 13°E) and altitudes (from 500 to 6000 m). All parcels started from the plane of the cross-section shown in Fig. 2. Parcels were launched at 01 and 06 UTC.

The accurate calculation of trajectories from hourly model data requires considerable care. Particularly at low altitudes, it was necessary to use a short 20 s time step to obtain consistent results. Even so, a few trajectories are found to intersect the terrain. Forward trajectories were checked against reverse trajectories. The paths of parcels released at two levels (1500 and 4000 m) are shown in Fig. 6. Those launched from 1500 m moved north-west before turning northward and crossing the Alps. All parcels that reached 48°N were analysed for their changes in potential temperature, mixing ratio and equivalent potential temperature. To evaluate the thermodynamic consistency of the trajectory computation, we compared the drying and heating. In moist adiabatic flow, the relationship between changes in water (Δq) and heat ($\Delta \theta$) is:

$$\Delta\theta = -(\theta/T)(L/C_p)\Delta q, \tag{11}$$

so that the equivalent potential temperature,

$$\theta_E = \theta \exp(Lq/C_p T), \tag{12}$$

is approximately conserved. With q expressed in g kg^{-1}, the coefficient in (11) is about -2.7 K g^{-1}kg (for liquid). A linear regression of $\Delta\theta$ versus Δq for the trajectory end points gives a slope of -2.5 K g^{-1}kg with small scatter. The changes in equivalent potential temperature were small, typically less than 1 K. These checks add confidence to the trajectories. The scatter could be due to model errors, trajectory errors or non-conservative physical processes such as the melting of hydrometeors, cloud-top radiation or boundary-layer heating.
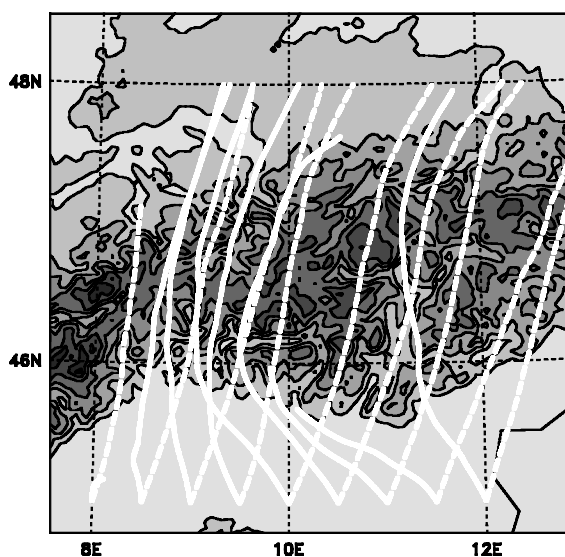
Figure 6.   Trajectories for IOP 2b computed from the COAMPS model. Parcels are launched from altitudes of 1500 m (solid) and 4000 m (dashed) at 06 UTC 20 September 1999. Terrain (shaded) has a contour interval of 500 m. Lower-level parcels move westward before crossing the Alps. See text for details.

Two examples of trajectories launched from an altitude of 1500 m are shown in Fig. 7. The western parcel (longitude 8.5°E) rose 2000 m while losing 4 g kg^{-1} of water and warming 8 K; during this rise it reached the freezing level at 3700 m. Downstream of the Alpine ridge, the parcel descended about 500 m and gained some moisture by evaporation of cloud water. A later lifting event, 200 km downstream of the ridge, dried and warmed the air further. No significant lee-side descent occurred.

The eastern parcel (longitude 12°E) lifted only slightly, oscillating over rough terrain, and then descended to very low levels along the lee slope of the Alps. This parcel behaviour would give rise to a pre-frontal southerly föhn in Bavaria. The net change in heat and moisture over the whole trajectory is very small. The dry föhn character on the lee slope was caused more by descent from a higher altitude than by upslope precipitation (see Seibert 1990). Neither trajectory exhibited the classical behaviour of moist ascent and dry descent.

The relationship between parcel warming and launch altitude for all the 06 UTC trajectories is shown in Fig. 8(a). The 01 UTC launches show a similar pattern. The scatter is unexpectedly large due in part to the differences between the western, central and eastern launches. The low-level western launches show parcel warming of nearly 10 K. At higher altitudes the parcel warming is small, or even slightly negative. The central and eastern launches show much less warming, akin to the example in Fig. 7(b). Further, a significant number of parcels above the freezing level (3700 m) are cooled and moistened during their cross-mountain transit. Cooling as great as 4 K is noted for a few of the parcels launched between 4 and 6 km. The removal of heat from these parcels appears to be caused by the sublimation of blowing snow in the middle troposphere as air descends over the northern slope of the Alps. Note also that no abnormality is present at or below the freezing level at 3800 m. This may indicate that hydrometeor melting is not strongly influencing the temperature of air parcels (see Marwitz 1987).

The warming of air parcels is remarkably well correlated with the total change in altitude during the transit (Fig. 8(b)). The slope of this correlation line can be expressed
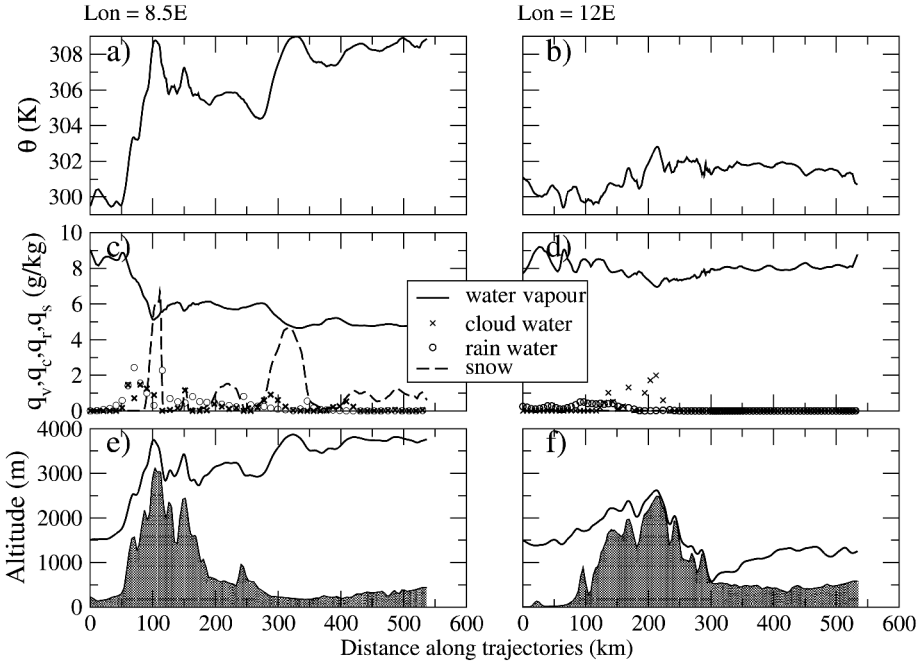
Figure 7. Properties of two COAMPS model trajectories launched from an altitude of 1500 m, at 45.5°N, 8.5 and 12°E at 06 UTC 20 September 1999: (a) and (b) potential temperature of the parcels, (c) and (d) specific humidities, cloud water, rain and snow, (e) and (f) altitudes of the parcels and the underlying terrain. The density values for condensed species in (c) and (d) are doubled for better visibility. See text for details.
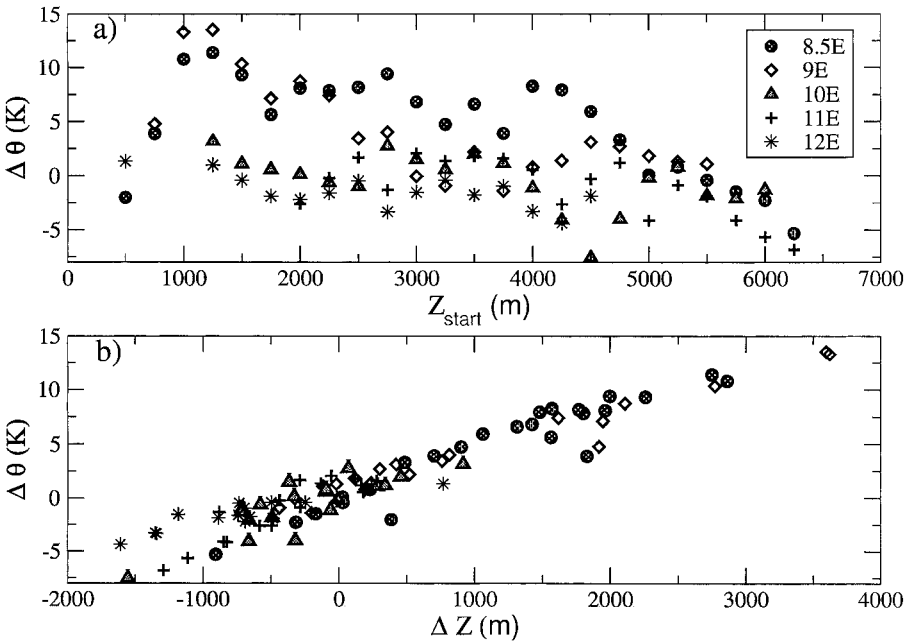

Figure 8. Air mass warming and lifting for all COAMPS model trajectories of parcels launched at 45.5°N and at 06 UTC 20 September 1999 that reach 48°N, showing longitudes of origin: (a) change in potential temperature versus launch altitude; (b) net parcel rise versus parcel warming. Parcel warming is seen to be well correlated with net parcel rise. See text for details of model.

TABLE 4. QUANTITIES IN EQ. (13)

Symbol	Definition	Value
P	Precipitation (see Table 1)	30×10^6 kg s^{-1}
L_c	Latent heat of condensation	2.5×10^6 kg^{-1}K^{-1}
ρ	Average air density	1.0 kg m^{-3}
C_p	Heat capacity of air at constant pressure	1004×10^6 J kg^{-1}K^{-1}
u	Mean wind speed	15 m s^{-1}
H	Depth of heated layer	5 km
W	Lateral width of heated layer	178 km
$\Delta\theta$	Average warming	5.6 K

as a potential-temperature lapse rate of about 3.8 K km^{-1}. This slope applies to parcels that have cooled or warmed by moist thermodynamics; the slope of 3.8 is approximately the slope of the moist adiabat for these temperatures. It is also close to the typical observed lapse rate in midlatitudes. One can imagine that with a large variability in the warming and cooling over the Alps (Fig. 8(a)), the parcels must sort themselves out by potential temperature on the lee side: parcels with a larger $\Delta\Theta$ will rise buoyantly relative to others, to find an equilibrium level; parcels cooled by the sublimation of snow must descend. The net result is a surprising scrambling of the air parcels crossing the Alps. Parcels launched from lower levels may end up higher than parcels that start higher. This scrambling should be considered part of the air mass transformation process.

Finally, we compare the heating of parcels with estimates of bulk heating using the data from section 3. A control volume analysis over the mountain yields a relationship between precipitation rate and air mass heating.

$$\Delta\theta = PL_c/\rho C_p UHW, \tag{13}$$

where the symbols are given in Table 4.

Using values corresponding to the COAMPS precipitation in Box A from 00 to 12 UTC, the average heating is 5.6 K. This value fits generally in the range of heating found in the trajectory calculations (Fig. 8). The simple nature of (13) however, masks the complex and highly variable nature of air mass transformation seen in the trajectories.

6. DOMINANT SPACE- AND TIME-SCALES: MONTE LEMA RADAR

A final set of questions concerns the dominant space- and time-scales of orographic precipitation. While the Alpine massif is more than 100 km across, the mesoscale models indicate that the structure of precipitation has a smaller-scale, closer to 10 or 20 km (Fig 3). The models seem to be responding mostly to smaller elements in the Alpine terrain. To test this prediction, and to examine temporal fluctuations, we used data from the Monte Lema Doppler radar located south of Lago Maggiore (see appendix). Our analysis is qualitative only; we make no attempt to deduce calibrated rain rates or microphysical properties.

The four panels in Fig. 9 show the 24 h precipitation accumulations from three models and the radar observations for a small region centred on Monte Lema. This region nearly coincides with the southern half of Box A shown in Fig. 1. The radar resolves the precipitation over the first mountain range, south-east and south-west of Monte Lema. Local reflectivity maxima are also present over a second mountain range near $y = 25$ km, both north-east and north-west of the radar station. Precipitation onto a third mountain range is seen at $x = -70$, $y = 50$. The northern part of the radar
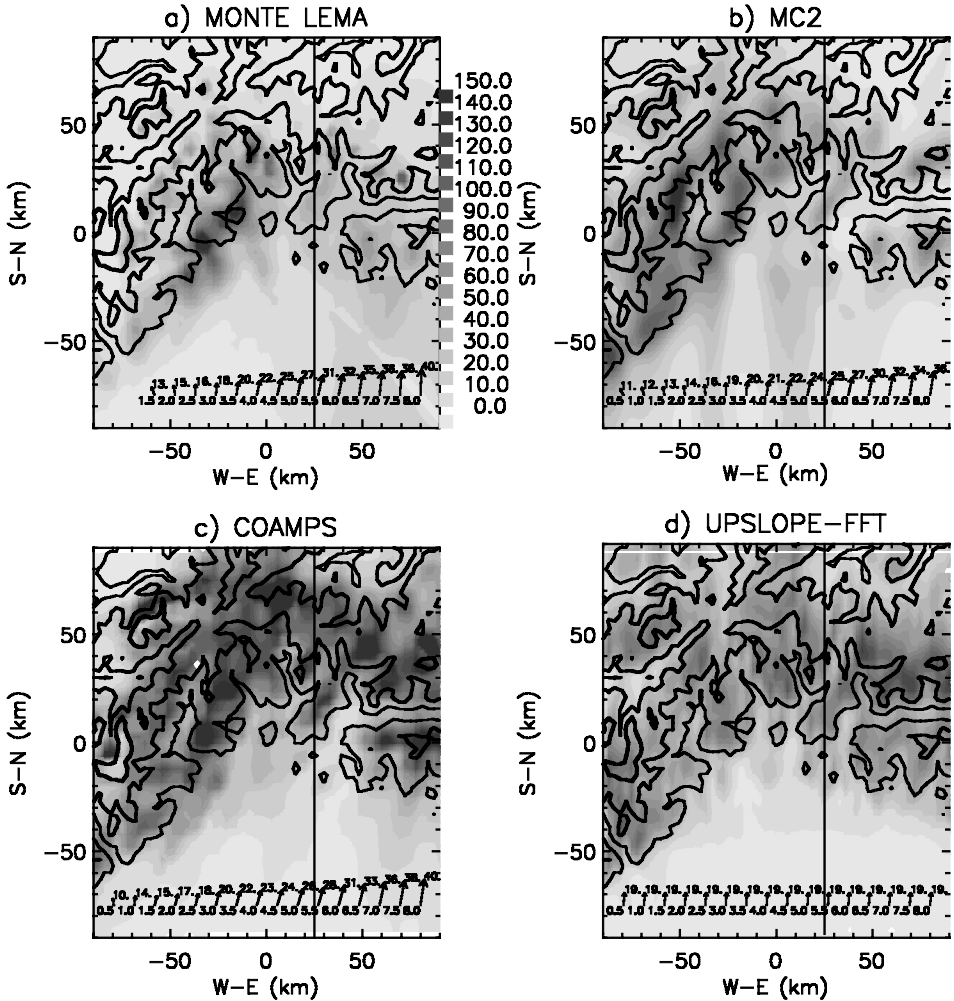
Figure 9. Plan view of a region near the Monte Lema radar (46.042°N, 8.833°E). Distances are km from the radar. Accumulated precipitation (mm, see key) for 20 September 1999 from: (a) radar; and models (b) COAMPS, (c) MC2, (d) UTD (with $T_c = T_f = 500$ s, $U = -1.7$, $V = 19.1$ m s^{-1}, divided by 10). Corresponding wind profiles are shown at the bottom of each frame. The vertical line 25 km east of the radar marks the location of the cross-sections in Figs. 10 and 11. See text for further details.

domain shows little precipitation, due to the blocking of the beam by higher mountains. The upstream region, south of the radar, is well observed. It shows small amounts of precipitation in the south-eastern sector and none in the south-west. The overall impression is of strong local orographic control on scales as small as 10 km.

The MC2 precipitation field shows maxima over the first, second and third mountain ranges, in agreement with the radar. It captures the decreased precipitation in the valleys between the ranges. It also shows the south-to-north path of convective systems in the upstream region, but it puts these paths in the south-west rather than the south-east corner as shown by the radar (see also Gheusi 2001). The COAMPS precipitation pattern is similar to the MC2 pattern, but with larger amounts.

The UTD model prediction in Fig. 8(d) is derived by using Doppler radar winds from the Monte Lema site, independent of any mesoscale model. This wind profile is
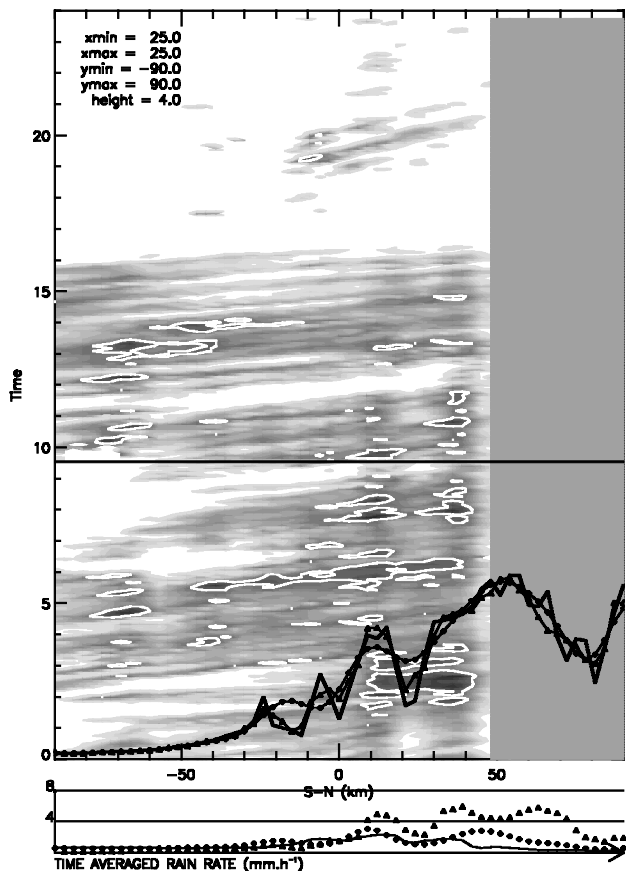
Figure 10.   Time (UTC) versus distance diagram of Monte Lema radar reflectivity along 9.15°E at 4 km altitude for 20 September 1999. Measurements are every 7.5 minutes. Orographic precipitation locked to the terrain dominates until 16 UTC. Unsteadiness in the precipitation over terrain is associated with many small drifting disturbances that amplify over the hills. The downstream edge of the pattern near $x = 50$ km is an artifact due to terrain screening of the radar. The time-averaged precipitation rates from extrapolated radar data (solid line), and mesoscale models COAMPS (triangles) and MC2 (diamonds) are shown at the bottom of the figure. Terrain for the two models is also shown. See text for details.

averaged vertically up to 5 km and the result, $U = 1.7$, $V = 19.1$ m s^{-1}, is used in (1) and (2) along with a terrain field smoothed to 3 km. The specific humidity in (1) is specified as a function of altitude from a saturated adiabat. The time delays used in this calculation are 500 s. The agreement between the UTD model, the mesoscale models and the radar data is reasonably good. The UTD model puts the precipitation maxima over the peaks and captures the minima in the valleys.

Some insight into the physical processes producing the small-scale precipitation patterns can be seen by examining radar reflectivity in a vertical cross-section. We chose a north–south reference line at 9.25°E, located 25 km east of the radar. The space–time pattern of reflectivity at $z = 4$ km is illustrated with a Hovmüller diagram in Fig. 10. The striking feature of this diagram is the drifting of reflective features that develop upwind. The two maxima over the hills at $y = 10$ and 35 km are due to the amplification of these drifting features. Similar patterns have been noted over smaller hills by Browning *et al.* (1974) and Hill *et al.* (1981). The time interval between the pulses is typically about 15 minutes. Higher-frequency fluctuations may be present, but are not resolved
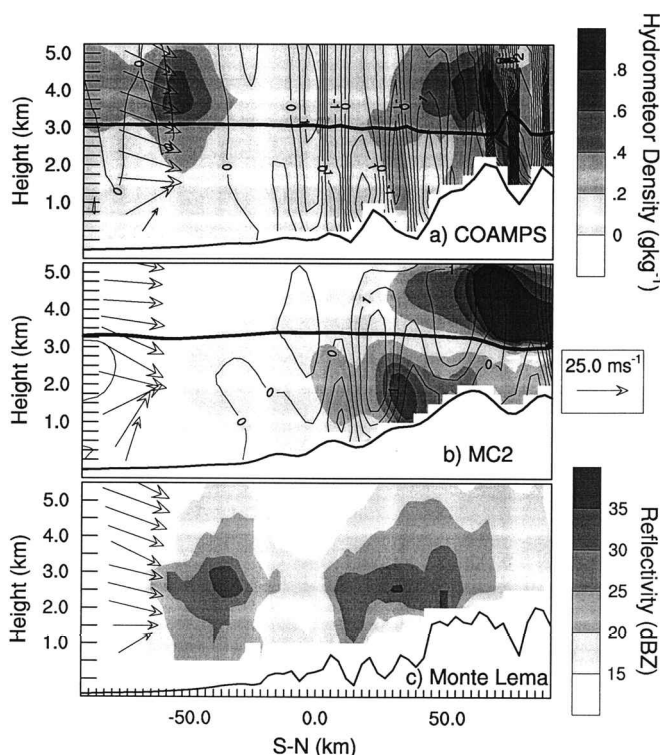
Figure 11. Vertical cross-sections along 9.25°E at 08 UTC 20 September 1999 for models: (a) COAMPS and (b) MC2, vertical motion (contoured) and total hydrometeor density (shaded), with the predicted freezing level (bold line) and upstream wind profile; (c) reflectivity (shaded) from the Monte Lema radar and the upstream wind profile determined from conical Doppler scans. Both models capture the turning wind profile from south-easterlies at low altitude to south-westerlies aloft.

by our 5-minute sampling frequency. The observed precipitation ceases at 16 UTC, in agreement with the model time series in Fig. 4. A brief convective event occurred at 19 UTC. The sharp decrease in reflectivity beyond $y = 45$ km is an artifact of radar beam blockage by terrain.

The vertical distribution of hydrometeors along the 9.15°E section is shown in Fig. 11. The time of the section is 08 UTC which, as seen in Fig. 10, falls in the period of quasi-steady orographic precipitation. However, this is still a 'snapshot' of a time-varying field (see Fig. 10). In Figs. 11(a) and (b) the model terrain, vertical velocity, freezing level and hydrometeor density are shown. The wind speed and direction at the position of Monte Lema are shown by arrows in the left-hand part of the diagrams. In Fig. 11(c), the observed reflectivity is shown, along with the Doppler wind profile above the Monte Lema radar. Several types of comparison can be made using this figure.

The three wind profiles in Fig. 11 are in approximate agreement. Below 2 km the wind direction is south-easterly, shifting to southerly or south-westerly aloft. The freezing level in the models is about 3.8 km. The abrupt rise in reflectivity in Fig. 11(c) below 3.5 km can be interpreted as the bright-band arising from melting hydrometeors, but low-level precipitation enhancement may also be present (Hill *et al.* 1981). The vertical velocities in both models are clearly topographic in origin. They coincide with the terrain slope. COAMPS has stronger vertical velocity, penetrating to higher altitudes than MC2. The MC2 fields are smoother due to the slightly smoother terrain

representation. The general pattern of vertical motion provides some support for the assumptions of the UTD model (1).

The model hydrometeor fields can only be compared qualitatively with the radar-reflectivity fields, due to bright-band effects and temporal change. Generally, the hydrometeor shafts are shifted slightly downstream from the upslope regions. This shifted pattern may be caused by time delays in hydrometeor formation and fall-out. The hydrometeor fields in the two models do not agree very well, except that both respond to small-scale terrain. COAMPS has more rain at low levels and much more snow above the freezing line.

7. CONCLUSIONS

The objective of this study is to develop new diagnostic methods for describing orographic air mass transformation. As we rely heavily on model data, we used two models, COAMPS and MC2, to evaluate their reliability.

The comparison of the two models found many points of agreement: the time sequence of incoming water vapour fluxes, the dominant scale of the precipitation pattern, the prediction of evening convection, the wind profile near Monte Lema, the freezing level, and the deep patterns of terrain-induced vertical motion. When winds and humidities from the two models are used in the UTD model (1), they give similar rates of cloud-water generation. The models differ most in their microphysics. The COAMPS gives higher densities of rain and snow and more precipitation. MC2 gives higher cloud-water densities.

We also note that the ECMWF model predictions and analyses give estimates of water vapour fluxes and precipitation that agree with the mesoscale model estimates for this case. This may increase confidence in using global models to examine the role of mountains on regional climate.

The focus of the paper is the process of orographic precipitation and air mass transformation. On the largest scale the picture seems fairly simple. The incoming 'jet' of water vapour associated with the approaching front is mostly confined below 3 km. About 35% of this flux is rained out on the southern slopes of the Alps. Estimates of precipitation efficiency (*PE*) vary widely because our estimates of condensation rate are scale- and method-dependent. For a smooth uplift scenario, *PE* is nearly 100%. If small-scale terrain is included, the condensation rate is much larger, even exceeding the incoming water vapour flux, and the corresponding *PE* is very low. These residence times for condensed water ranged mostly from 500 to 2000 s. With a 20 m s^{-1} wind speed, this residence time allows 10 to 40 km of drift, consistent with the smaller-scale spatial patterns observed in the models.

The buoyant work over the mountains was computed as an indicator of classical föhn versus thermal convection. The sign of this quantity changed during the study period, indicating a shift towards convection.

Trajectory calculations provided a Lagrangian view of orographic air mass transformation. The picture is complex; none of the trajectories exhibited the textbook pattern of moist ascent and dry descent. Those that gained latent heat while rising continued to rise on the lee side. Those parcels that descended along the lee slope came from mid-levels upstream and gained little heat diabatically. At high levels a dominant cooling was found. Downstream, parcels with different heating histories ascended or descended to reach buoyant equilibrium. The resulting scrambling of air parcels should be part of our conceptual picture of air mass transformation.

The three models, COAMPS, MC2 and UTD, and the radar data, indicate that the dominant physical scale of precipitation is between 10 and 20 km, even though the north–south width of the Alpine massif is a factor of ten greater. The smaller-scale complex terrain within the Alpine range is dominating the physical processes of uplift, condensation, conversion and fallout. The bulk process of air mass transformation is a composite of processes occurring on smaller scales.

The temporal analysis of Monte Lema radar data indicates that the small-scale orographic precipitation is not in pure steady state. The precipitation appears to occur due to the terrain enhancement of frequent small-scale drifting reflective patches that form tens of km upstream. These patches may arise from upstream lifting of an inhomogeneous incoming water vapour field. We did not attempt to see if the models captured this high-frequency activity.

In a companion paper, the vertical profile of air mass transformation has been shown to influence the dynamics of waves and downslope flow on the lee side of the Alps in this case (Doyle and Smith 2003). The decrease in static stability above 5 km traps lee waves, and tunes the atmosphere to a nonlinear resonant hydrostatic response. The result is plunging flow, föhn and strong lee waves on the north side of the eastern Alps. Thus, airflow dynamics and air mass transformation are linked.

APPENDIX

Processing of radar data

The radar used for the present study is the Swiss C-band Monte Lema radar located in the Alpine southern upslope region. Its sampling strategy is extensively described in Joss *et al.* (1998). The position and the sampling characteristics of the radar are given in Table A.1.

Once corrected for ground clutter and correctly edited, these data were interpolated onto a Cartesian grid centred on the radar using a Cressman filter. The domain of the radar analysis was square with horizontal dimensions of 180 km by 180 km. The height of the analysed box was 12 km. The grid size was 3 km in the horizontal direction and 0.5 km in the vertical direction. The horizontal and vertical Cressman radii vary linearly from 3 and 0.5 km close to the radar to 6 and 1 km at 100 km away from the radar. Those values (grid meshes, grid sizes and Cressman radii) were chosen so as to optimize the coverage within the grid while maintaining the spatial resolution of the interpolated fields consistent with the purposes of the present work.

We also used the best estimates of the rain rates at the ground provided by the Swiss Meteorological Institute. This dataset is obtained from the 5-minute reflectivity data, but a number of corrections and vertical extrapolations are applied (Joss and Lee 1995; Joss *et al.* 1998; and Vignal *et al.* 2000).

The wind profiles in Fig. 11 were obtained by Tabary and Petitdidier (2002) using a modified Bayesian velocity–azimuth display analysis. These wind profiles were quality

TABLE A.1.   THE MONTE LEMA RADAR

Characteristic	Value
Latitude	46.042°N
Longitude	8.833°E
Altitude a.m.s.l.	1625 m
Frequency	5.6 GHz and 45 MHz
Elevation Angles	0.3, 0.5, 1.5, 2.5, 3.5, 4.5, 5.5, 6.5, 7.5, 8.5, 9.5, 11, 13, 15.5, 18.3, 21.6, 25.3, 29.6, 34.5, 40
Scan period	5 minutes
Gate spacing/width	1 km
Azimuthal resolution	1 degree
30 dB beam width	1 degree

checked and compared with simultaneous wind-profiler measurements. Each profile starts at the height of 1500 m (approximately the height of the radar) and extends up to the top of reflectivity echoes. The vertical grid spacing is 500 m, which is consistent with the grid spacing of the Cartesian grid used for the reflectivity values.

REFERENCES

Benoit, R., Desgagne, M., Pellerin, P., Pellerin, S., Chartier, Y. and Desjardins, S.   1997   The Canadian Mc2: A semi-Lagrangian semi-implicit wide-band atmospheric model suited for finescale process studies and simulation. *Mon. Weather Rev.*, **125,** 2382–2415

Benoit, R., Schar, C., Binder, P., Chamberland, S., Davies, H. C., Desgagne, M., Girard, C., Keil, C., Kouwen, N., Luthi, D., Maric, D., Muller, E., Pellerin, P. and Schmidli, J.   2002   The real-time ultrafinescale forecast support during the Special Observing period of the MAP. *Bull. Am. Meteorol. Soc.*, **83,** 85–109

Bergeron, T.   1960   *Physics of precipitation*. American Geophysical Union, Washington DC, USA

Bougeault, P., Binder, P., Buzzi, A., Dirks, R., Houze, R., Kuettner, J. P., Smith, R. B., Steinacker, R. and Volkert, H.   2001   The MAP special observing period. *Bull. Am. Meteorol. Soc.*, **82,** 433–462

Browning, K. A., Hill, F. F. and Pardoe, C. W.   1974   Structure and mechanism of precipitation and the effect of orography in a wintertime warm sector. *Q. J. R. Meteorol. Soc.*, **100,** 309–330

Bruintjes, R. T., Clark, T. L. and Hall, W. D.   1994   Interactions between topographic airflow and cloud/precipitation development during the passage of a winter storm in Arizona. *J. Atmos. Sci.*, **51**(1), 48–67

Buzzi, A., Tartaglione, N. and Malguzzi, P.   1998   Numerical simulations of the 1994 Piedmont flood: Role of orography and moist processes. *Mon. Weather Rev.*, **126,** 2369–2383

Colle, B. A., Westrick, K. J. and Mass, C. F.   1999   Evaluation of MM5 and Eta-10 precipitation forecasts over the Pacific Northwest during the cool season. *Weather and Forecasting*, **14,** 137–154

Doswell, C. A., Ramis, C., Romero, R. and Alonso, S.   1998   A diagnostic study of three heavy precipitation episodes in the western Mediterranean region. *Weather and Forecasting*, **13,** 102–124

Doyle, J. D. and Smith, R. B.   2003   Mountain waves over the Hohe Tauern: Influence of upstream diabatic effects, *Q. J. R. Meteorol. Soc.*, **129,** 799–823

Ferretti, R., Low-Nam, S. and Rotunno, R.   2000   Numerical simulations of the Piedmont flood of 4–6 November 1994. *Tellus*, **52A**(2), 162–180

Frei, C. and Schär, C.   1998   A precipitation climatology of the Alps from high-resolution rain-gauge observations. *Int. J. Climatol.*, **18**(8), 873–900

Gheusi, F.	2001	'Analyses Eulériennes et Lagrangiennes des systèmes convectifs quasi-stationnaires sur les Alpes'. Doctoral thesis. Université Toulouse III - Paul Sabatier, Toulouse (available from Centre National de Recherches Météorologiques, Météo-France, 42 avenue G. Coriolis, 31057 Toulouse Cedex, France)
Haimberger, L., Hantel, M. and Dorninger, M.	1995	A thermodynamic diagnostic model for the atmosphere. Part III: DIAMOD with orography and new error model. *Meteorol. Zeitschrift*, **4**, 162–182
Hill, F. F., Browning, K. A. and Bader, M. J.	1981	Radar and rain-gauge observations of orographic rain in south Wales. *Q. J. R. Meteorol. Soc.*, **107**, 643–670
Hodur, R. M.	1997	The Naval Research Laboratory's Coupled Ocean/Atmosphere Mesoscale Prediction System (COAMPS). *Mon. Weather Rev.*, **125**, 1414–1430
Jiang, Q.	2001	Some theoretical aspects of orographic precipitation. PhD Thesis. Yale University, New Haven
Jiang, Q. and Smith, R. B.	2003	Cloud time scales and orographic precipitation. *J. Atmos. Sci.*, in press
Joss, J. and Lee, R.	1995	The application of radar–gauge comparisons to operational precipitation profile corrections. *J. Appl. Meteorol.*, **34**, 2612–2630
Joss, J., Schädler, B., Galli, G., Cavalli, R., Bosacci, M., Held, E., della Bruna, G., Kappenberger, G., Nespor, V. and Spiess, R.	1998	'Operational use of radar for precipitation measurements in Switzerland'. Final report NRP 31, vdf Hochschule AG an der ETH Zürich, Switzerland
Kong, Y. and Yau, M. K	1997	An explicit approach to microphysics in MC2. *Atmos–Ocean*, **35**, 257–291
Kuligowski, R. J. and Barros, A. P.	1999	High-resolution short-term quantitative precipitation forecasting in mountainous regions using a nested model. *J. Geophys. Res.*, **104**(D24), 31553–31564
Marwitz, J. D.	1987	Deep orographic storms over the Sierra Nevada. Part 2: Precipitation processes. *J. Atmos. Sci.*, **44**(1), 174–185
Mellor, G. L. and Yamada, T.	1974	Hierarchy of turbulence closure models for planetary boundary layers. *J. Atmos. Sci.*, **31**(7), 1791–1806
Mladek, R., Barckicke, J., Binder, P., Bougeault, P., Brzovic, N., Frei, C., Geleyn, J. F., Hoffman, J., Ott, W., Paccagnella, T., Patruno, P., Pottier, P. and Rossa, A.	2000	Intercomparison and evaluation of precipitation forecasts for MAP seasons 1995 and 1996. *Meteorol. Atmos. Phys.*, **72**(2–4), 111–129
Rauber, R. M.	1992	Microphysical structure and evolution of a central Sierra Nevada orographic cloud system. *J. Appl. Meteorol.*, **31**(1), 3–24
Rotunno, R. and Ferretti, R.	2001	Mechanisms of intense Alpine rainfall. *J. Atmos. Sci.*, **58**(13), 1732–1749
Rutledge, S. A. and Hobbs, P. V.	1983	Mesoscale and microscale structure and organization of clouds and precipitation in midlatitude cyclones. Part 8: A model for the seeder-feeder process in warm-frontal rainbands. *J. Atmos. Sci.*, **40**(4), 1185–1206
Schneidereit, M. and Schär, C.	2000	Idealised numerical experiments of Alpine flow regimes and southside precipitation events, *Meteorol. Atmos. Phys*, **72**(2–4), 233–250
Seibert, P.	1990	South föhn studies since the ALPEX experiment, *Meteorol. Atmos. Phys.*, **43**(1–4), 91–103
Smith, R. B.	1979	The influence of mountains on the atmosphere. *Adv. Geophys.*, **21**, 87–230
	2003	A linear upslope-time-delay model for orographic precipitation. *J. Hydrol.,* in press
Smith, R. B., Skubis, S., Doyle, J. D., Broad, A., Volkert, H. and Kiemle, C.	2002	Mountain waves over Mt. Blanc: The role of a stagnant boundary layer. *J. Atmos. Sci.*, **59**, 2073–2092
Tabary, P. and Petitdidier, M.	2002	Application of a Bayesian wind-profile retrieval technique to radar data collected in the Alpine southern upslope region and comparison with upstream wind profiler measurement. *J. Atmos. Oceanic Technol.*, **19**(6), 875–887

Vignal, B., Galli, G., Joss, J. and   2000   Three methods to determine profiles of reflectivity from volu-
    Germann, U.   metric radar data to correct precipitation estimates. *J. Appl.
                                                       Meteorol.*, **39,** 1715–1726
Young, K. C.   1974   A numerical simulation of wintertime orographic precipitation.
                                                   Part I: Description of model micro physics and numerical
                                                   technique. *J. Atmos. Sci.*, **31,** 1735–1748